



Full length article

# Synergistic effect of heteroatom-doped activated carbon for ultrafast charge storage kinetics

Dong-Yo Shin<sup>a</sup>, Ki-Wook Sung<sup>b</sup>, Hyo-Jin Ahn<sup>a,b,\*</sup><sup>a</sup> Program of Materials Science & Engineering, Convergence Institute of Biomedical Engineering and Biomaterials, Seoul National University of Science and Technology, Seoul 01811, Republic of Korea<sup>b</sup> Department of Materials Science and Engineering, Seoul National University of Science and Technology, Seoul 01811, Republic of Korea

## ARTICLE INFO

## Keywords:

Ultrafast electrical double-layer capacitors  
 Charge storage kinetics  
 Heteroatom doping  
 Activated carbon  
 Synergistic effect

## ABSTRACT

Providing a crystallographic and electronic modification of carbon-based materials in electrical double-layer capacitors (EDLCs) is an essential technology needed to improve the charge storage kinetics and to enhance ultrafast cycling performances. However, despite numerous structural composite and morphological modification efforts focused on active materials, ultrafast charge storage kinetics still indicated a poor ultrafast capacitance and low cycling stability. To solve these problems, in the present study, we propose a novel heteroatom (N, P, and B)-doped activated carbon (AC) that has the synergistic effects of N-, P-, and B-doping using the one-pot doping calcination process. Compared to the bare-AC, N-doped AC, P-doped AC, and B-doped AC, the novel heteroatom-doped AC indicates an improved ultrafast charge storage kinetics, such as high specific capacitance ( $243.9 \text{ F g}^{-1}$  at the scan rate of  $10 \text{ mV s}^{-1}$ ), good cycling stability ( $216.7 \text{ F g}^{-1}$  at  $100 \text{ mV s}^{-1}$  after 500 cycles), and superb ultrafast cycling capacitance ( $199.7 \text{ F g}^{-1}$  at  $300 \text{ mV s}^{-1}$ ). These superb electrochemical performances can be attributed by synergistic effects of increased active sites by N-doping related to a high charge storage area, improved functional groups by P-doping related to an excellent wettability between the electrode and the electrolyte, and enhanced electrical properties by B-doping related to a good electron acceptability.

## 1. Introduction

In recent years, due to their several advantages over conventional secondary batteries such as higher power density, faster charge/discharge rate, and longer life times than conventional secondary batteries electrochemical capacitors (ECs) have come into wide use in portable devices, electric vehicles, high-power equipment, and memory back-up devices [1–4]. In general, the ECs can be generally categorized into three types by energy storage mechanisms [5–7]: (1) electrical double-layer capacitors (EDLCs) that operate with a physical adsorption/desorption of charge between the carbon-based materials and the electrolyte (non-Faradaic reaction); (2) pseudo capacitors (PCs) that act by the redox reaction between metal oxide-based material and the electrolyte (Faradaic reaction); and (3) hybrid capacitors that drive by the combination of non-Faradaic and Faradaic reaction. Among these energy storage mechanisms, EDLCs have outstanding advantages, such as high power density, long life times, high-rate capability, and low cost [8]. However, despite these advantages, EDLCs have limitations of low energy density ( $5\text{--}15 \text{ Wh kg}^{-1}$ ) and high-rate performance of carbon-

based materials as the electrode has a low active site, a poor wettability between the electrode and the electrolyte, and restrictive electrical property. Therefore, to overcome these problems, various strategies, including improvement of porous structure related to energy density, adjustment of surface functional group related to wettability, and introduction of dopant related to electrical conductivity, have been attempted [9,10]. Particularly attractive strategies in this respect are the functional group adjustment and the dopant introduction, as they can improve the ultrafast charge storage kinetics. For example, to enhance the wettability between the electrode and the electrolyte, Lai et al. synthesized the pyrrole-coated reduced graphene oxide (rGO). The authors reported that, due to the increased reaction rate by a high accessibility of electrolyte, pyrrole-coated rGO indicated a high capacitance ( $150 \text{ F g}^{-1}$ ) with a good cycling stability [11]. Furthermore, to improve the electrical properties of carbon, Lee et al. fabricated manganese-doped carbon aerogel. The authors found that, due to enhanced charge transfer rate by high electrical conductivity, the sample displayed a high capacitance ( $125 \text{ F g}^{-1}$ ) with an excellent cycling stability [12]. However, the synergistic effect of heteroatom introduction in

\* Corresponding author at: Program of Materials Science & Engineering, Convergence Institute of Biomedical Engineering and Biomaterials, Seoul National University of Science and Technology, Seoul 01811, Republic of Korea.

E-mail address: [hjahn@seoultech.ac.kr](mailto:hjahn@seoultech.ac.kr) (H.-J. Ahn).

<https://doi.org/10.1016/j.apsusc.2019.01.186>

Received 30 August 2018; Received in revised form 20 December 2018; Accepted 22 January 2019

Available online 24 January 2019

0169-4332/ © 2019 Elsevier B.V. All rights reserved.

carbon-based materials has not yet been precisely certified for the ultrafast charge storage kinetics in EDLCs. Therefore, the synergistic effect of heteroatom-doped activated carbon (AC) as electrode material is essentially required for the ultrafast EDLCs. In the present study, we propose the synergistic effect of boron (B), phosphate (P), and nitrogen (N) application in AC for ultrafast charge storage kinetics in EDLCs.

## 2. Experiments

The N-, P-, and B-doped AC as electrode material was successfully synthesized using the one-pot doping calcination. To synthesize the N-, P-, and B-doped AC, bare-AC (99.99%, Power Carbon Technology) was mixed with 1 M nitric acid ( $\text{HNO}_3$ , 66%, SAMCHUN), 1 M phosphorus red (red P, 98.5%, ALADDIN), and 1 M boric acid ( $\text{H}_3\text{BO}_3$ , 99.5%, SAMCHUN) in DI-water at 3000 rpm for 30 min using the planetary ball milling. Thereafter, the mixed solution was dried at 100 °C for 12 h. The doping calcination was performed using a tube furnace at 900 °C for 6 h in the argon (99.999%) atmosphere. In the next step, all doping agents were removed by acid treatment using a mixture of hydrogen fluoride (HF, 52%, SAMCHUN) and hydrofluoric acid (HCl, 52%, SAMCHUN). The N-, P-, and B-doped AC is henceforth referred to as NPB-AC. For comparison, the AC doped with N, P, or B, respectively, was fabricated using the above-mentioned method (referred to herein as N-AC, P-AC, and B-AC, respectively).

The morphology and structural characteristics of all samples were analysed using field emission-scanning electron microscopy (FESEM, Hitachi S-4800) and Energy-dispersive X-ray spectrometry mapping (EDS-mapping). The crystal structure and chemical bonding state were investigated using X-ray diffraction (XRD, Rigaku D/MAX2500 V) and X-ray photoelectron spectroscopy (XPS, ESCALAB 250 used with an Al  $K_{\alpha}$  X-ray source). Furthermore, the electrochemical performances were measured using a conventional three-electrode system composed of a working electrode (glassy carbon), a counter electrode (Pt wire), and a reference electrode (Ag/AgCl saturated KCl solution). The electrode slurry was prepared by the mixture of a Ketjen black (Mitsubishi Chemical, ECP-600JD) as the conducting material, poly(vinylidenedifluoride) (PVDF, Alfa Aesar) as the binder, and the samples as the active material in the weight ratio of 8:1:1 in *N*-methyl-2-pyrrolidinone (NMP, 99.5%, Aldrich). All slurry was applied on glassy carbon and dried at 60 °C for 1 h in a conventional oven. Finally, cyclic voltammetry (CV) analyses were conducted at the scan rates of 10, 30, 50, 100, 200, 300  $\text{mV s}^{-1}$  in the potential range of 0.0–1.0 V.

## 3. Results and discussion

Fig. 1a-e shows the FESEM images of bare-AC, N-AC, P-AC, B-AC, and NPB-AC, respectively. The morphology of bare-AC did not have any specific shape and did not significantly change after the N-, P-, and B-

doping process. The diameters of the bare-AC, N-AC, P-AC, B-AC, and NPB-AC indicated ca. 6.2–9.7  $\mu\text{m}$ , 6.0–9.6  $\mu\text{m}$ , 5.9–9.9  $\mu\text{m}$ , 6.0–9.7  $\mu\text{m}$ , and 5.8–9.5  $\mu\text{m}$ , respectively. In addition, according to the results of the SEM-EDS mapping (see Fig. 1f), N, P, and B elements uniformly had the atomic percent of 7.6, 5.1, and 5.8%, respectively. In particular, the atomic percent of O increased sharply from 5.1 to 23.6% due to the formation of O-containing functional groups ( $-\text{O}$ ,  $\mu\text{OH}$ , and  $=\text{O}$ ) by heteroatoms doping [13,14]. The O-containing functional groups were previously reported to improve the electrochemical performance by the increased wettability of the electrolyte [6]. In addition, due to the increased active site by the heteroatom doping, the specific surface area ( $2520.4 \text{ m}^2 \text{ g}^{-1}$ ) and the total pore volume ( $1.88 \text{ cm}^3 \text{ g}^{-1}$ ) of NPB-AC were higher than the specific surface area ( $2186.1 \text{ m}^2 \text{ g}^{-1}$ ) and the total pore volume ( $0.97 \text{ cm}^3 \text{ g}^{-1}$ ) of bare-AC (see Fig. S1a). Especially, pore diameter and pore volume are increased compared to bare-AC because it has the highest specific surface area and highest total pore volume (see Fig. S1b).

Fig. 2 shows a schematic illustration of N-, P-, and B-doping site in a graphene lattice structure of graphite. In Fig. 2a, the N atoms have three different configurations of graphitic-N (or quaternary-N), pyrrolic-N, and pyridinic-N in the graphene lattice plane [15,16]. Pyridinic-N atoms are formed at the edges of the graphene lattice plane bonded to two C atoms with the generation of one  $\pi$ -electron by  $\pi$  electron systems. Pyrrolic-N atoms are located at the heterocyclic rings of the graphene lattice plane coupled with two C atoms, offering two  $\pi$ -electrons by  $\pi$  electron systems [16]. In the case of graphitic-N, they are located by the replacement of the C atoms to N atoms in the graphene lattice plane. It appears that the N atom could locally modulate the electronic properties of the graphene lattice plane, as the electronegativity of N atom (3.04) was reported to be higher than that of the C atom (2.55) [15–18]. It could offer strong bonds with C atoms (N–C bond) by a smaller atomic size of N than the atomic size of C. In addition, as reported in previous research, pyridinic-N and pyrrolic-N offer the active site, which can improve the electrochemical performance by turning off the C–C bonds with extra  $\pi$ -electron [17,18]. The P atoms in the graphene lattice plane show four different structures of  $\text{PC}_2\text{O}_2$ ,  $\text{PCO}_2$ ,  $\text{PC}_2\text{O}$ , and  $\text{PCO}_3$  (see Fig. 2b) [19]. In general, P atoms have been known to form the coordination of three, four, or five atoms in the graphene lattice structure, when the P atoms replace the carbon located two edge, and it generate the oxygen-containing functional groups ( $-\text{O}$ ,  $=\text{O}$ , and  $-\text{OH}$ ) [8,20]. The oxygen-containing functional groups were reported to enhance the electrochemical performance because they facilitate the connection of the charge from the improved wettability of the electrolyte [8,19,20]. The B atoms appeared in four different types of  $\text{BCO}_2$ ,  $\text{B}_4\text{C}$ ,  $\text{BC}_3$ , and  $\text{BCO}_3$  due to replacement of B into the C  $\text{sp}^2$  frame (see Fig. 2c) [21,22]. In addition, the B atoms cause a transition of the electronic structure and electronic density state of the C atoms, suggesting the Faradic reaction and initiating a higher value of

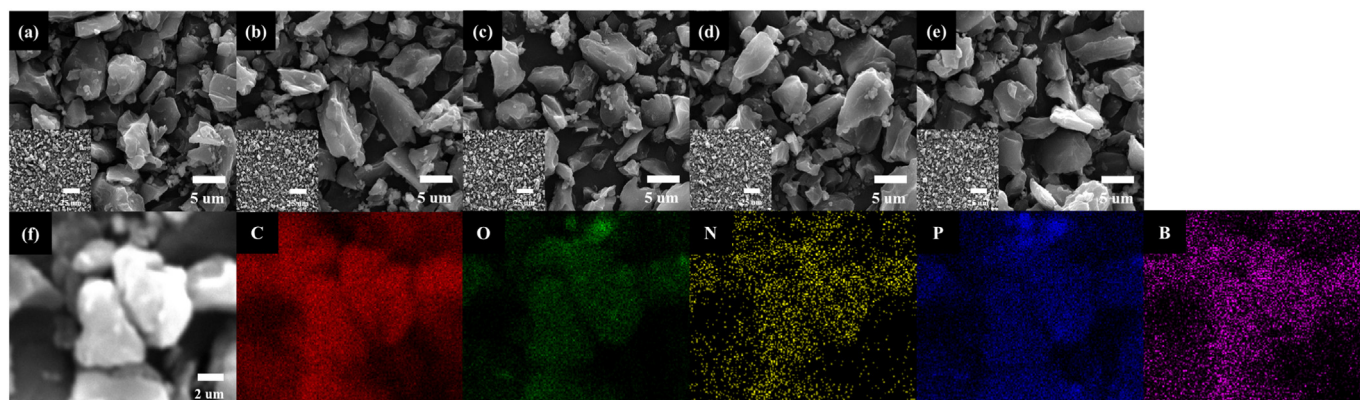


Fig. 1. (a-e) FESEM images of bare-AC, N-AC, P-AC, B-AC, and NPB-AC and (f) SEM-EDS mapping result of NPB-AC.

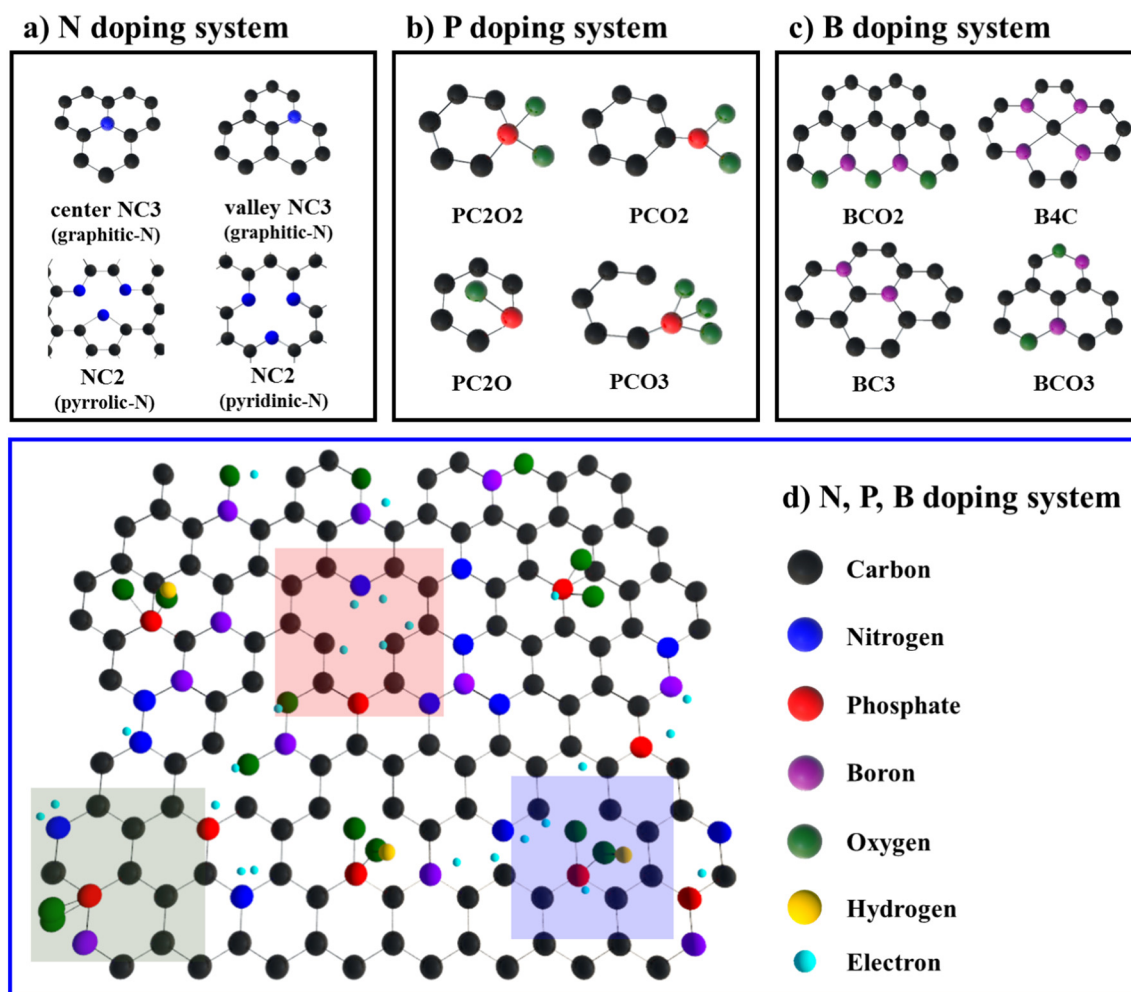


Fig. 2. Schematic illustration of N, P, and B doping system in graphene lattice structure.

the interfacial capacitance [23]. The B–O bond is formed by electronic state transformation at the edge of the graphene lattice structure [23]. Therefore, N-, P-, and B-doped carbon indicates the synergistic doping structure, including the improved active site by N-doping, the increased functional groups by P-doping, and the enhanced electron accepting by B-doping [24,25]. Thus, N-, P-, and B-doped carbon shows a combination doping effect of N, P, B atoms, including increased active sites, improved functional groups, and enhanced electron acceptability (see Fig. 2d) [24,25].

To confirm the doping state of N, P, and B atoms on the AC, the XPS measurements were performed (see Fig. 3a–f). Fig. 3a shows the XPS full scan spectrum of NPB-AC confirming the presence of C, O, N, P, and B atoms with no other elements. The C 1s spectrum of NPB-AC (see Fig. 3b) shows a typical signal at ~284.0, ~284.6, ~286.1, ~287.5, ~288.7, and ~290.5 eV, corresponding to different bonding states of C–B, C–C, C–O or –N, or –P, C–O–C, C–O–B, and  $\pi-\pi^*$ , respectively [24,25]. In particular, the C–B, C–N, and C–P bonding are well known to be formed by the replacement of the C element of C–C bonding to B, N, and P atoms [26]. The O 1s XPS spectrum of NPB-AC (see Fig. 3c) shows four signals at ~530.9, ~532.1, ~533.1, and ~535.0 eV, corresponding to the C–O or P–O, –OH, O–C=O, and COOH bonding, respectively [26,27]. Generally, since P atoms can form three-, four-, or five-atom coordination in the graphene lattice structure, the P–O bonding is formed by a replacement of the two-edge C element by the P element [8,19]. The formed O-containing functional groups (–O, =O, and –OH) can improve the capacitance of electrode material by facilitating the connection of the charge from the enhanced wettability of

the electrolyte [8,19,20]. In addition, the N 1s XPS spectrum of NPB-AC (see Fig. 3d) exhibits three signals at ~398.3, ~399.5, and ~401.0 eV, corresponding to the pyridinic-N, graphitic-N, and pyrrolic-N bonding state [16,18]. In general, due to breaking the bonds of C, the pyridinic-N and pyrrolic-N contribute to the increasing active site. The pyridinic-N and pyrrolic-N, formed at the edge of graphene lattice structure with a bonding of two C atoms, offer one and two p-electron by aromatic  $\pi$  system [15–18]. The P 2p spectrum of NPB-AC (see Fig. 3e) exhibits two signals at 133.0 and 135.0 eV, corresponding to P–C and P–O bonding states, respectively [28,29]. The P–O bonding state was formed at the edge of the graphene lattice structure by O-containing functional groups. In addition, the B 1s (see Fig. 3f) signal indicated three types of BCO<sub>2</sub>, BC<sub>2</sub>O, and BC<sub>3</sub> states at the binding energy of 190, 191.3, and 192.5 eV, respectively. Due to a changed band gap and an adjusted Fermi-level depression, the B atoms exchanged the C atoms with a modification of the electronic structure and enhanced the electron acceptability [30,31]. Therefore, the doped N, P, and B in AC were successfully confirmed by the results of the XPS analyses.

Electrochemical performances were measured using a conventional three-electrode system in the 0.5 M H<sub>2</sub>SO<sub>4</sub> electrolyte. Fig. 4a–e shows the cyclic voltammetry (CV) curves for bare-AC, N-AC, P-AC, B-AC, and NPB-AC. All samples were measured at the scan rates of 10, 30, 50, 100, 200, and 300 mV s<sup>–1</sup> in the potential range of 0.0–1.0 V. The CV curve area of all samples increased with an increase of the scan rate, meaning a decrease in the specific capacitance by the limited diffusion of ions in the electrolyte [8]. The CV curve of the bare-AC (see Fig. 4a) shows a semi-rectangular behavior, indicating ideal EDLC behavior. On the

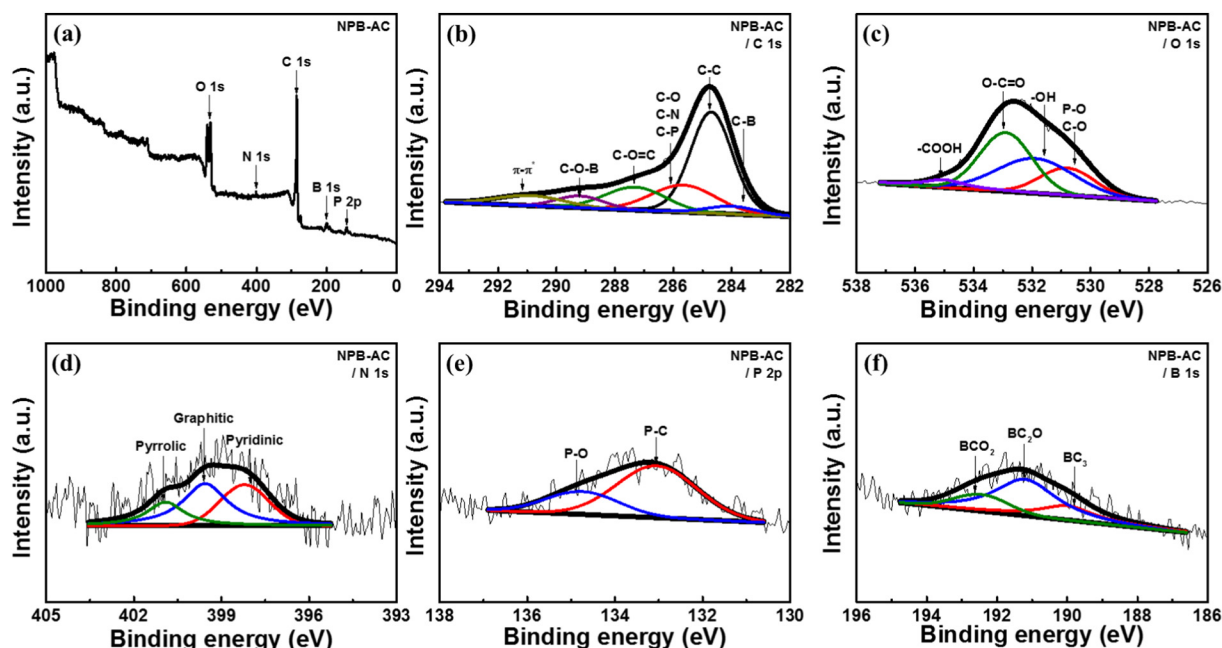


Fig. 3. XPS results of (a) full scan spectrum of NPB-AC and XPS spectra obtained from (b) C 1s, (c) O 1s, (d) N 1s, (e) P 2p, and (f) B 1s of NPB-AC.

other hand, the N-AC (see Fig. 4b) shows the redox peak at 0.37 and 0.47 V due to the formation of N-containing functional group of N–C [32]. The CV curve of the P-AC (see Fig. 4c) shows a redox peak at 0.44 and 0.11 V, as it caused the O-containing functional groups (P–O, P–OH, and P=O) by formed P-doping in the graphene lattice structure [33]. In addition, the redox peaks of B-AC in the CV curve (see Fig. 4d) are observed at 0.39 and 0.12 V, indicating a lower redox peak intensity as compared to that of N-AC and P-AC. Due to the formation of functional groups, the dominant B-doping effect in the graphene lattice structure modifies the electronic state of C, rather than the increase of redox reaction, thereby improving the electron acceptability [34]. In particular, the CV curve of NPB-AC (see Fig. 4e) exhibits as a combination of CV curves of N-AC, P-AC, and B-AC, with the largest CV area among the samples.

Fig. 5(f) shows the specific capacitance of bare-AC, N-AC, P-AC, B-AC, and NPB-AC at various scan rates shown in Fig. 5a–e. The specific capacitances ( $C$ ) were calculated using Eq. (1) [12]:

$$C = (Q_c + Q_a)/(2m\Delta V) \quad (1)$$

where  $Q_c$  and  $Q_a$  are the charges obtained from integrated cathodic and anodic areas in the CV curves,  $m$  is the mass of the active materials, and  $\Delta V$  is the potential range of the CV curves. At  $10 \text{ mV s}^{-1}$ , the specific capacitance values of bare-AC, N-AC, P-AC, B-AC, and NPB-AC were 198.8, 227.1, 217.6, 203.8, and  $243.9 \text{ F g}^{-1}$ , respectively. Due to the diffusion limitation of the ion and the electron, the N-AC and P-AC show a high capacitance at the low scan rate of  $10 \text{ mV s}^{-1}$  while a large capacitance reduction with an increase of the scan rate from 10 to  $300 \text{ mV s}^{-1}$  [8]. On the other hand, the B-AC displays a poor capacitance at a low scan rate, but it shows an excellent capacitance retention at the high scan rate of  $300 \text{ mV s}^{-1}$  due to improved electron acceptability [21,22]. Among the samples, the NPB-AC exhibited the highest specific capacitance, as well as a high rate capacitance ( $199.7 \text{ F g}^{-1}$ ) at  $300 \text{ mV s}^{-1}$ . This result is higher than previously reported values for doped carbon-based materials in EDLCs (see Table S1). In addition, the cycling stability of NPB-AC ( $216.7 \text{ F g}^{-1}$  with the capacitance retention

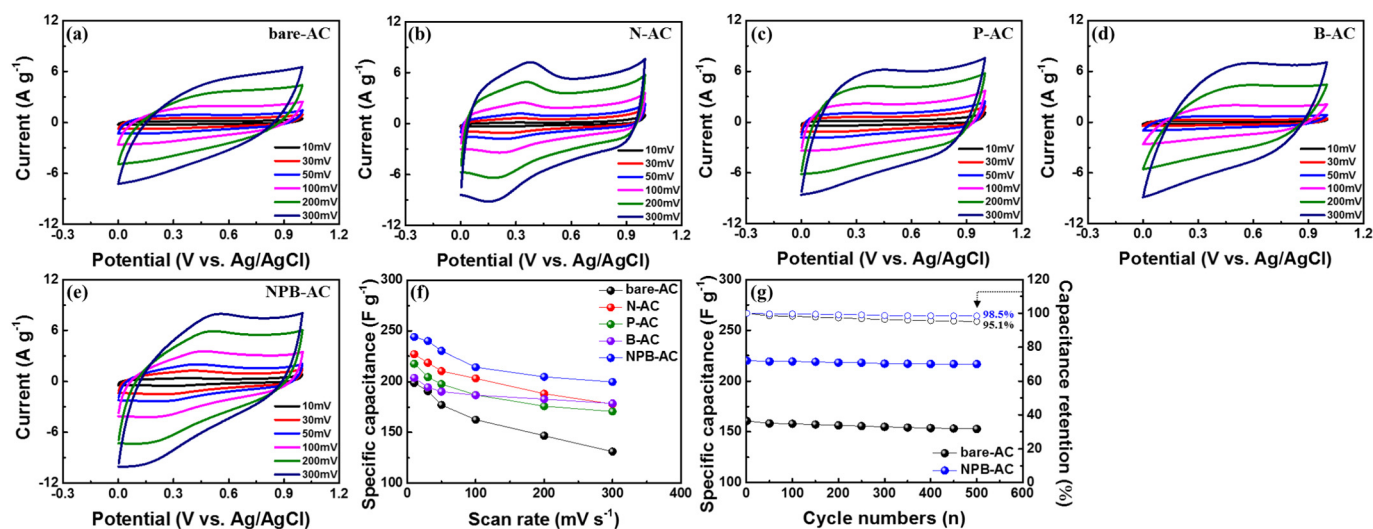


Fig. 4. Cyclic voltammetry of (a) bare-AC, (b) N-AC, (c) P-AC, (d) B-AC, and (e) NPB-AC characterized at scan rate from  $10 \text{ mV s}^{-1}$  to  $300 \text{ mV s}^{-1}$  in the potential range of 0.0–1.0 V. (e) specific capacitance of all samples calculated from their CVs. (f) cycling stability test of all samples at  $100 \text{ mV s}^{-1}$  measured up to 500 cycles.

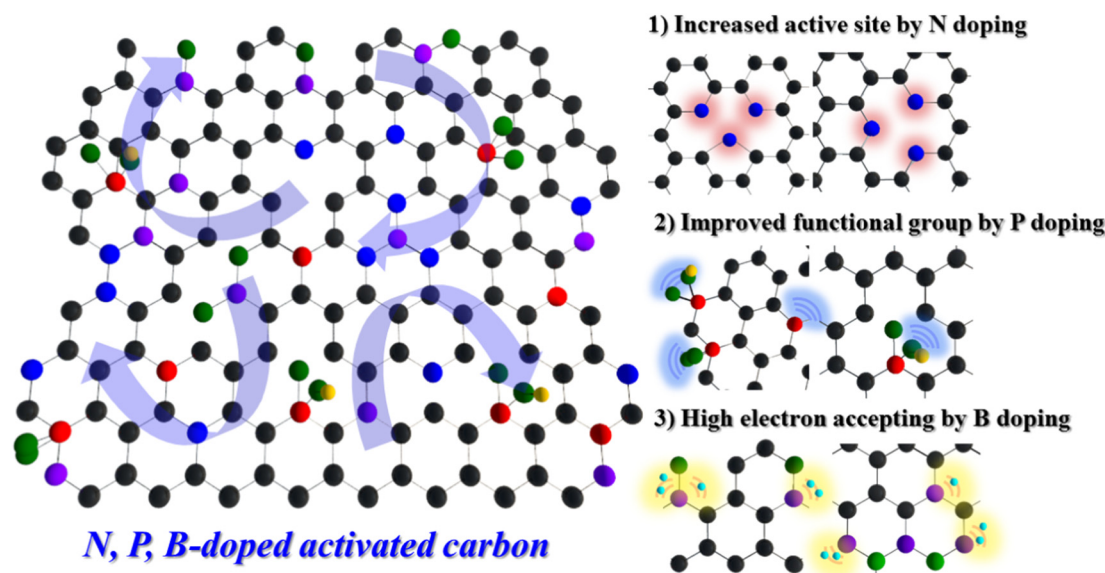


Fig. 5. Schematic illustration of three synergistic effects of N, P, and B doping for enhanced ultrafast cycling performances.

of 98.5%) was higher than that of bare-AC ( $152.8 \text{ F g}^{-1}$  with the capacitance retention of 95.1%) at  $100 \text{ mV s}^{-1}$  after 500 cycles (see Fig. 4g).

Therefore, in our study, the improved electrochemical performance with charge storage kinetics was achieved by doping the heteroatom into AC. Thus, the observed enhanced electrochemical performances can be attributed to three main effects. First, an increase of active area on the surface by N doping enables an efficient charge storage, leading to an increased specific capacitance. Second, the improvement of functional groups by P-doping can yield excellent wettability between the electrode and the electrolyte, leading to cycling stability. Third, enhancement of electrical properties by B-doping can reinforce a fast electron acceptability, leading to ultrafast charge storage kinetics. Based on these results, it can be concluded that the NPB-AC exhibits superb charge storage kinetic at a high scan rate and has excellent specific capacitance with cycling stability (see Fig. 5).

#### 4. Conclusions

In the present study, the heteroatom (N, P, and B)-doped AC for ultrafast EDLCs was successfully fabricated using the doping calcination. The atomic percent of N, P, and B in AC amounted to 7.6, 5.1, and 5.8%, respectively with a high O atomic percent (23.6%). The improved electrochemical performances of NPB-AC were investigated; in the results, we observed a high specific capacitance ( $243.9 \text{ F g}^{-1}$  at the scan rate of  $10 \text{ mV s}^{-1}$ ), an excellent cycling stability ( $216.7 \text{ F g}^{-1}$  with the capacitance retention of 98.5% at the scan rate of  $100 \text{ mV s}^{-1}$  after 500 cycles), and a superb ultrafast cycling capacitance ( $199.7 \text{ F g}^{-1}$  at the scan rate of  $300 \text{ mV s}^{-1}$ ). These improvements can be attributed to the following three main effects: (1) a high specific capacitance can be attributed to an increased active site by N-doping, which effectively provides a charge storage site; (2) the superb cycling stability is related to the improved functional groups by P-doping, providing an enhancement of wettability between the electrode and the electrolyte; (3) the excellent ultrafast cycling capacitance can be ascribed to advanced electrical properties by B-doping, corresponding to a high electron acceptability. Taken together, the results of the present study suggest that the synergistic effects of heteroatom doping in AC is a promising strategy for practical applications of ultrafast EDLCs.

#### Acknowledgement

This work was supported by the Technology Innovation Program (10080656, Development of ceramic/carbon convergence and integration anode material for 10C fast charging Lithium ion battery) funded by the Ministry of Trade, Industry & Energy (MOTIE, Korea).

#### Appendix A. Supplementary data

Supplementary data to this article can be found online at <https://doi.org/10.1016/j.apsusc.2019.01.186>.

#### References

- [1] Y. Ko, M. Kwon, W.K. Bae, B. Lee, S.W. Lee, J. Cho, Flexible supercapacitor electrodes based on real metal-like cellulose papers, *Nat. Commun.* 8 (2017) 1–11.
- [2] L. Zhang, F. Zhang, X. Yang, G. Long, Y. Wu, T. Zhang, K. Leng, Y. Huang, Y. Ma, A. Yu, Y. Chen, Porous 3D graphene-based bulk materials with exceptional high surface area and excellent conductivity for supercapacitors, *Sci. Rep.* 3 (2013) 1–9.
- [3] M. Chen, S. Zhao, S. Jiang, C. Huang, X. Wang, Z. Yang, K. Xiang, Y. Zhang, Suppressing the polysulfide shuttle effect by heteroatom-doping for high-performance lithium-sulfur batteries, *ACS Sustain. Chem. Eng.* 6 (2018) 7545–7557.
- [4] M. Chen, S. Jiang, C. Huang, X. Wang, S. Cai, K. Xiang, Y. Zhang, J. Xue, Honeycomb-like nitrogen and sulfur dual-doped hierarchical porous biomass carbon for high-energy-density lithium-sulfur batteries, *ChemSusChem* 10 (2018) 1803–1812.
- [5] G.H. An, B.R. Koo, H.J. Ahn, Activated mesoporous carbon nanofibers fabricated using water etching-assisted templating for high-performance electrochemical capacitors, *Phys. Chem. Chem. Phys.* 18 (2016) 6587–6594.
- [6] G.H. An, D.Y. Lee, H.J. Ahn, Vanadium nitride encapsulated carbon fibre networks with furrowed porous surfaces for ultrafast asymmetric supercapacitors with robust cycle life, *J. Mater. Chem. A* 5 (2017) 19714–19720.
- [7] H. An, Y. Wang, X. Wang, N. Li, L. Zheng, The preparation of PANI/CA composite electrode material for supercapacitors and its electrochemical performance, *J. Solid State Electrochem.* 14 (2010) 651–657.
- [8] D.Y. Shin, I.K. Park, H.J. Ahn, Enhanced electrochemical performance of phosphorus incorporated carbon nanofibers by the spin-on dopant method, *RSC Adv.* 6 (2016) 58823–58830.
- [9] Z. Zhao, M. Li, L. Zhang, L. Dai, Z. Xia, Design principles for heteroatom-doped carbon nanomaterials as highly efficient catalysts for fuel cells and metal-air batteries, *Adv. Mater.* 27 (2015) 6834–6840.
- [10] Y. Yao, H. Chen, J. Qin, G. Wu, C. Lian, J. Zhang, S. Wang, Iron encapsulated in boron and nitrogen codoped carbon nanotubes as synergistic catalysts for fenton-like reaction, *Water Res.* 101 (2016) 281–291.
- [11] L. Lai, L. Wang, H. Yang, N.G. Sahoo, Q.X. Tam, J. Liu, C.K. Poh, S.H. Lim, Z. Shen, J. Lin, Tuning graphene surface chemistry to prepare graphene/polypyrrole supercapacitors with improved performance, *Nano Energy* 1 (2012) 723–731.
- [12] Y.J. Lee, J.C. Jung, S. Park, J.G. Seo, S.H. Baeck, J.R. Yoon, J. Yi, I.K. Song, Preparation and characterization of metal-doped carbon aerogel for supercapacitor, *Curr. Appl. Phys.* 10 (2010) 947–951.
- [13] R. Li, Z. Wei, X. Gou, W. Xu, Phosphorus-doped graphene nanosheets as efficient

- metal-free oxygen reduction electrocatalysts, *RSC Adv.* 3 (2013) 9978–9984.
- [14] F. Niu, L.M. Tao, Y.C. Deng, Q.H. Wang, W.G. Song, Phosphorus doped graphene nanosheets for room temperature NH<sub>3</sub> sensing, *New J. Chem.* 38 (2014) 2269–2272.
- [15] H. Liu, Y. Zhang, R. Li, X. Sun, S. Desilets, H.A. Rachid, M. Jaidann, L.S. Lussier, Structural and morphological control of aligned nitrogen-doped carbon nanotubes, *Carbon* 48 (2010) 1794–1507.
- [16] T. Sharifi, G. Hu, X. Jia, T. Wagberg, Formation of active sites for oxygen reduction reactions by transformation of nitrogen functionalities in nitrogen-doped carbon nanotubes, *ACS Nano* 6 (2012) 8904–8912.
- [17] J.W.F. To, J. He, W. Mei, R. Haghpanah, Z. Chen, T. Kurosawa, S. Chen, W.G. Bae, L. Pan, J.B.H. Tok, J. Wilcox, Z. Bao, Hierarchical N-doped carbon as CO<sub>2</sub> adsorbent with high CO<sub>2</sub> selectivity from rationally designed polypyrrole precursor, *J. Am. Chem. Soc.* 138 (2016) 1001–1009.
- [18] G.A. Ferrero, K. Preuss, A. Marinovic, A.B. Jorge, N. Mansor, D.J.L. Brett, A.B. Fuentes, M. Sevilla, M.M. Titirici, Fe–N-doped carbon capsules with outstanding electrochemical performance and stability for the oxygen reduction reaction in both acid and alkaline conditions, *ACS Nano* 10 (2016) (5992–5932).
- [19] W. Yang, W. Yang, L. Kong, A. Song, X. Qin, G. Shao, Phosphorus-doped 3D hierarchical porous carbon for high-performance supercapacitors: a balanced strategy for pore structure and chemical composition, *Carbon* 127 (2018) 557–567.
- [20] M.Q. Guo, J.Q. Huang, X.Y. Kong, H.J. Peng, H. Shui, F.Y. Qian, L. Zhu, W.C. Zhu, Q. Zhang, Hydrothermal synthesis of porous phosphorus-doped carbon nanotubes and their use in the oxygen reduction reaction and lithium-sulfur batteries, *New Carbon Mater.* 31 (2016) 352–362.
- [21] M. Wang, Y. Yang, Z. Yang, L. Gu, Q. Chen, Y. Yu, Sodium-ion batteries: improving the rate capability of 3D interconnected carbon nanofibers thin film by boron, nitrogen dual-doping, *Adv. Sci.* 4 (2017) 1600468.
- [22] C. Wang, Z. Guo, W. Shen, Q. Xu, H. Liu, Y. Wang, B-doped carbon coating improves the electrochemical performance of electrode materials for Li-ion batteries, *Adv. Funct. Mater.* 24 (2014) 5511–5521.
- [23] Z. Zhou, A. Wakamiya, T. Kushida, S. Yamaguchi, Planarized triarylboranes: stabilization by structural constraint and their plane-to-bowl conversion, *J. Am. Chem. Soc.* 134 (2012) 4529–4532.
- [24] P. Routh, S.H. Shin, S.M. Jung, H.J. Choi, I.Y. Jeon, J.B. Baek, Boron-nitrogen-phosphorous doped graphene nanoplatelets for enhanced electrocatalytic activity, *Eur. Polym. J.* 99 (2018) 511–517.
- [25] H. Lin, L. Chu, X. Wang, Z. Yao, F. Liu, Y. Ai, X. Zhuang, S. Han, Boron, nitrogen, and phosphorous ternary doped graphene aerogel with hierarchically porous structures as highly efficient electrocatalysts for oxygen reduction reaction, *New J. Chem.* 40 (2016) 6022–6029.
- [26] M.K. Barman, B. Jana, S. Bhattacharyya, A. Patra, Photophysical properties of doped carbon dots (N, P, and B) and their influence on electron/hole transfer in carbon dots – nickel (II) phthalocyanine conjugates, *J. Phys. Chem. C* 118 (2014) 20034–20041.
- [27] S. Yang, L. Peng, P. Huang, X. Wang, Y. Sun, C. Cao, W. Song, Nitrogen, phosphorus, and sulfur co-doped hollow carbon shell as superior metal-free catalyst for selective oxidation of aromatic alkanes, *Angew. Chem.* 128 (2016) 4084–4088.
- [28] R. Li, Z. Wei, X. Gou, W. Xu, Phosphorus-doped graphene nanosheets as efficient metal-free oxygen reduction electrocatalysts, *RSC Adv.* 3 (2013) 9978–9984.
- [29] H. Zhang, X. Li, D. Zhang, L. Zhang, M. Kapilashrami, T. Sun, P.A. Glans, J. Zhu, J. Zhong, Z. Hu, J. Guo, X. Sun, Comprehensive electronic structure characterization of pristine and nitrogen/phosphorus doped carbon nanocages, *Carbon* 103 (2016) 480–487.
- [30] B. Wei, R. Spolenak, P.K. Redlich, M. Ruhle, E. Arzt, Electrical transport in pure and boron-doped carbon nanotubes, *Appl. Phys. Lett.* 74 (1999) 3149–3151.
- [31] L. Yang, S. Jiang, Y. Zhao, L. Zhu, S. Chen, X. Wang, Q. Wu, J. Ma, Y. Ma, Z. Hu, Boron-doped carbon nanotubes as metal-free electrocatalysts for the oxygen reduction reaction, *Angew. Chem. Int. Ed.* 50 (2011) 7132–7135.
- [32] M. Zhou, F. Pu, Z. Wang, S. Guan, Nitrogen-doped porous carbons through KOH activation with superior performance in supercapacitors, *Carbon* 68 (2014) (185–104).
- [33] J. Patino, N.L. Salas, M.C. Gutierrez, D. Carriazo, M.L. Ferrer, F.D. Monte, Phosphorus-doped carbon–carbon nanotube hierarchical monoliths as true three-dimensional electrodes in supercapacitor cells, *J. Mater. Chem. A* 4 (2016) 1251–1263.
- [34] X. Zhai, Y. Song, J. Kiu, P. Li, M. Zhong, C. Ma, H. Wang, Q. Guo, L. Zhi, In-situ preparation of boron-doped carbons with ordered mesopores and enhanced electrochemical properties in supercapacitors, *J. Electrochem. Soc.* 159 (2012) E177–E182.